Optical properties of $PbSe/Pb_{1-x}Mn_xSe$ multiple-quantum-well structures

Shu Yuan, Norbert Frank, and Günther Bauer
Institut für Halbleiterphysik, Johannes Kepler Universität Linz, A-4040 Linz, Austria

Michael Kriechbaum
Institut für Theoretische Physik der Universität Graz, A-8010 Graz, Austria
(Received 17 February 1994)

The electronic structure and optical properties of narrow-gap $PbSe/Pb_{1-x}Mn_xSe$ quantum-well structures are investigated experimentally and theoretically. The samples were grown by molecular-beam epitaxy along the (111) growth direction and were characterized by high-resolution x-ray diffraction, using triple-axis diffractometry. Their optical properties were investigated by transmission and photoconductivity experiments in the midinfrared range using Fourier-transform spectroscopy. The experimental data show that $PbSe/Pb_{1-x}Mn_xSe$ has a staggered band lineup which is in agreement with recent data on coherent anti-Stokes Raman-scattering experiments (Geist *et al.*), from which it was concluded that holes are confined in the PbSe and electrons in the $Pb_{1-x}Mn_xSe$ layers. The experimental absorption data are compared with calculated data based on a $\mathbf{k}\cdot\mathbf{p}$ envelope-function approach for the type-II superlattice band structure which yields the energy eigenstates, eigenfunctions, and oscillator strengths. The absorption constant is obtained from an integration over $\mathbf{k}$ space, and the refractive index from a Kramers-Kronig transformation. The calculated fundamental absorption coefficients are in good agreement with the experimental data. Agreement between experimental and theoretical results is best for a normalized conduction-band-offset range of $\Delta E_c/\Delta E_g = -0.4$ to -0.6 (± 0.2).

I. INTRODUCTION

PbSe-based multiple-quantum-well (MQW) structures such as $PbSe/Pb_{1-x}Eu_xSe$ or $PbSe/Pb_{1-x}Sr_xSe$ are of interest for the fabrication of tunable diode lasers[1,2] in the midinfrared range. Recently, a lasing operation at quite high lattice temperatures has been reported.[3–5] It was shown that the partial substitution of Pb by the transition-metal manganese increases the energy gap in the ternary compound $Pb_{1-x}Mn_xSe$ substantially as compared to PbSe.[6] Furthermore, this substitution of the group-IV element by a paramagnetic ion offers the possibility for studying exchange interactions between localized $3d$ electrons of the Mn ions and the mobile carriers in the conduction or valence bands. The band parameters of PbSe (Ref. 7) and of $Pb_{1-x}Mn_xSe$ ($x < 3\%$), which are many valley semiconductors with a direct gap at the L points of the Brillouin zone (BZ), were obtained from cyclotron resonance, interband magneto-optics,[8] and coherent anti-Stokes Raman-scattering (CARS) experiments.[9] Quite recently, information on the band offsets in $PbSe/Pb_{1-x}Mn_xSe$ ($x < 3\%$) MQW's was obtained from measurements of the g factors by using CARS.[9] Because of the strong influence of the exchange interaction on the value of the g factors, this method is quite useful for getting information on which one of the PbSe or $Pb_{1-x}Mn_xSe$ layers actually confines either the electrons or the holes. From the values of the g factors and their temperature and magnetic-field dependence, it turned out that, in such MQS's, the holes are confined in the PbSe layers, whereas the electrons are confined in the $Pb_{1-x}Mn_xSe$ layers. This fact demonstrates a staggered band lineup, with the valence-band edge of PbSe lying above that of $Pb_{1-x}Mn_xSe$.

In this paper, we present a study on the optical properties of $PbSe/Pb_{1-x}Mn_xSe$ MQW's with PbSe widths ranging from 42 to 185 Å and Mn contents from 0.8 to 1.6 %. In Sec. II, the molecular-beam epitaxy (MBE) growth of the samples is described as well as their structural characterization using high-resolution x-ray diffraction and reciprocal space mapping. In Sec. III, results of the theoretical superlattice (SL) band-structure calculations are presented using a standard $\mathbf{k}\cdot\mathbf{p}$ Hamiltonian for the lead salt compounds, involving an envelope-function approximation (EFA).[10] The band parameters of PbSe and $Pb_{1-x}Mn_xSe$ are used as input parameters. Results obtained by the EFA theory for the superlattice states at the center and at the edges of the superlattice (mini) Brillouin zones are shown as a function of the band offset.

For a fixed band offset, the EFA theory is used to calculate dispersion and wave functions throughout the superlattice BZ, for states belonging either to the longitudinal or oblique valleys. In Sec. IV, the optical properties (absorption constant and refractive index) are calculated in the region of the fundamental absorption. These data are compared with photoconductivity spectra and are further used for a calculation of the transmission based on the transfer-matrix method. The calculated spectra are compared with experimental transmission spectra obtained by Fourier-transform spectroscopy. The peculiarities of the staggered type-II band lineup, i.e., a spatially indirect superlattice, in comparison to a type-I band lineup, manifest themselves most drastically in the frequency dependence of the photoconductivity spectra for energies above the PbSe gap.

II. MOLECULAR-BEAM EPITAXY OF PbTe/$Pb_{1-x}Mn_xSe$ MQW's

The molecular-beam epitaxy growth was carried out in an MBE system and the details of the setup can be found in Ref. 11. For PbSe growth two different effusion cells have to be used. The first cell is filled with the PbSe compound, whereas the second cell contains Se for adjusting the stoichiometry of the growing film. For the growth of $Pb_{1-x}Mn_xSe$ a manganese effusion cell is additionally used to adjust the composition of the ternary compound.

Prior to the MQW growth of the quantum-well stack, a comparatively thick $Pb_{1-x}Mn_xSe$ buffer layer of a few μm and with $x \approx 1.6\%$ was grown on freshly cleaved (111) BaF_2 substrates at substrate temperatures of 350 °C. The x content in the $Pb_{1-x}Mn_xSe$ barrier layers is the same as in the buffer layer for samples A and B, whereas it is only 0.8% for sample C. Therefore, the $Pb_{1-x}Mn_xSe$ buffer layer is transparent in the spectral range of interest. The thickness of the buffer layer was chosen to be large enough to ensure a nearly complete strain relaxation of the epilayer in spite of the lattice mismatch of 1.32% for the $Pb_{1-x}Mn_xSe$ ($x = 1.6\%$) buffer layer with respect to the BaF_2 substrate. The lattice mismatch between the PbSe layers and the $Pb_{1-x}Mn_xSe$ layers is only 0.15% for the small x content of 1.6% [$a_{Pb_{1-x}Mn_xSe}$ (Å) $= 6.127 - 0.00580x$, Ref. 12]. With such a small mismatch, the thicknesses of the PbSe layers (for all samples $d_W \leq 200$ Å) are well below the critical layer thickness for this heterosystem. Therefore, the PbSe layers are fully tensile strained with respect to the $Pb_{1-x}Mn_xSe$ buffer and the layers in the MQW's.

In the following, experimental investigations of the three different MQW samples (see Table I) are described. The structural perfection of the buffer layers was checked in a high-resolution triple-axis x-ray diffractometer, having a channel cut two-reflection Ge(220) analyzer crystal in the secondary beam. Because of the small separation between the zeroth order superlattice and the buffer layer peaks, $\Delta\omega = 63$ arcsec along the ω axis, both high resolution ω-2Θ scans, as well as isointensity contour plots (i.e., reciprocal space maps[13]) of symmetric Bragg reflections had to be recorded for a detailed analysis of the samples. A typical full width at half maximum (FWHM) of about 40 arcsec for the 3 μm $Pb_{1-x}Mn_xSe$ buffer layers was observed in ω-2Θ diffraction curves, and can be compared with the FWHM's of a 3 μm thick PbSe buffer layer (15 arsec) or the BaF_2 substrate (12 arsec). In order to determine the exact SL periods D and the thicknesses of the PbSe quantum wells, which are of crucial importance for the determination of the band offsets (see below), these

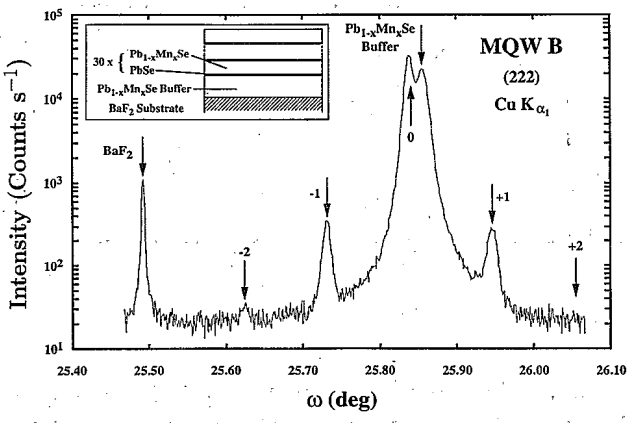

FIG. 1. High-resolution $\omega - 2\Theta$ x-ray diffraction pattern of sample MQW B, (222) Bragg reflection, Cu $K_{\alpha 1}$ radiation, which shows reflections from the BaF_2 substrate, the $Pb_{1-x}Mn_xSe$ buffer, and PbSe/$Pb_{1-x}Mn_xSe$ superlattice peaks as indicated.

diffraction experiments were performed on all MQW samples. As a representative example, we show the ω-2Θ scan (Fig. 1) and the reciprocal space map around the (222) Bragg reflection (Fig. 2) for MQW sample B.

In Fig. 1, in the ω-2Θ scan the zeroth order peak of the MQW stack can be clearly distinguished from the (222) Bragg peak of the $Pb_{1-x}Mn_xSe$ buffer layer, and the first and second order superlattice satellite peaks are observed as well. The superlattice period of the MQW stack was calculated from the spacing of the satellite peaks found in the ω-2Θ scans. By analyzing the x-ray contour plots of sample B (Fig. 2), the influences of lattice parameter deviations can be distinguished (e.g., strain gradients detected along the ω-2Θ axis) from that of mosaicity (detected along the ω axis), which contribute to the total FWHM observed in a rocking curve. The very broad peaks (FWHM > 300 arsec) usually found in the rocking curves of PbSe/$Pb_{1-x}Mn_xSe$ MQW samples result from a superposition of the intensities of the buffer layer and the zeroth order MQW peaks, and are mainly determined by the broadening due to mosaicity in the ternary IV-VI compound layers.[11] Measuring the symmetric (222) Bragg reflection at the same lateral position of a sample, but in different azimuths by rotating the sample around the surface normal leads to identical isointensity contour plots for both the BaF_2 substrate and the layer peaks, which proves that the orientation and the size of the mosaic blocks are isotropic. Consequently, the FWHM along the ω axis is not influenced by a curvature of the sample, which follows from the fact that the FWHM of the substrate peak is significantly smaller in the same

TABLE I. Sample parameters for the PbSe/$Pb_{1-x}Mn_xSe$ MQW's.

Sample index	$Pb_{1-x}Mn_xSe$ buffer (μm)	x-content buffer (%)	PbSe (Å)	$Pb_{1-x}Mn_xSe$ (Å)	x content (%)	Number of periods
A	3.01	1.5	180	269	1.5	30
B	2.91	1.6	42	253	1.6	30
C	3.34	1.6	185	277	0.8	30

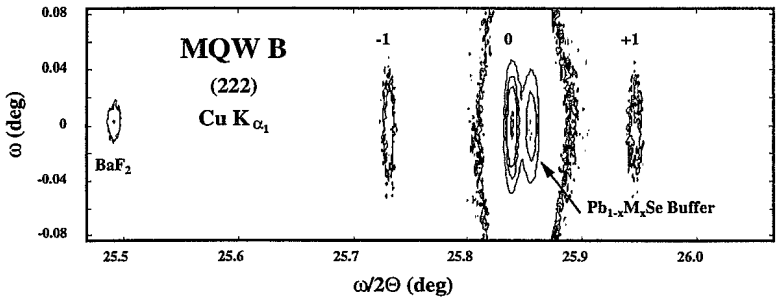

FIG. 2. Reciprocal map around the (222) Bragg reflection for sample MQW *B*. Contours of constant intensity are shown around the BaF_2 substrate, $Pb_{1-x}Mn_xSe$ buffer and $PbSe/Pb_{1-x}Mn_xSe$ superlattice reciprocal lattice points. Contours are shown for intensities 4, 6, 8, 400, 620, 800, and 1200 counts/sec.

direction. The Mn content in the $Pb_{1-x}Mn_xSe$ layers is calculated from the energy gap determined by temperature modulated transmission and photoconductivity measurements (see below) using the relationship between Mn content and the energy gap of $Pb_{1-x}Mn_xSe$ given in Ref. 6.

Temperature-dependent Hall measurements were performed on representative MQW samples. Because of the parallel conduction in the $Pb_{1-x}Mn_xSe$ barriers and the buffer layer, the Hall measurements are difficult to interpret. However, the low-temperature mobility of $Pb_{1-x}Mn_xSe$ decreases dramatically with increasing Mn content, similar to all ternary IV-VI compounds.[2,14] In thick single layer reference samples we get a Hall mobility of about $\mu = 400.000$ cm^2/V s for the electrons in bulk-like PbSe epilayers at $T = 20$ K, and an about a factor of 8 smaller value of $\mu = 50.000$ cm^2/V s for $Pb_{1-x}Mn_xSe$ ($x = 2\%$). In both cases the carrier concentration is of the order of $n = 5 \times 10^{17}$ cm^{-3}.

The structural parameters of the MQW samples *A*, *B*, and *C* which were used for further optical investigations are listed in Table I, as obtained from the characterization procedures described above.

III. ELECTRONIC PROPERTIES AND BAND OFFSETS OF $PbSe/Pb_{1-x}Mn_xSe$ STRUCTURES

From our recent magneto-optical investigations on $Pb_{1-x}Mn_xSe$ epitaxial layers it is known that the band structure of $Pb_{1-x}Mn_xSe$ is similar to that of PbSe.[8] Up to about 3% Mn content, the energy gap of $Pb_{1-x}Mn_xSe$ increases with x according to $E_g(Pb_{1-x}Mn_xSe) = 146$ meV + 3800 x (meV) at 4.2 K.[6] It turns out that such a calibration of the x content with the energy gap is not in quantitative agreement with the variation of the lattice constant in $Pb_{1-x}Mn_xSe$ as given by Koguchi, Takahashi, and Kiyosawa.[12]

The superlattice band structure in the vicinity of the band extrema at the L points of the BZ is calculated according to the procedure outlined by Kriechbaum *et al.*[10] and Yuan *et al.*[15] In the following, we present as an example in Fig. 3 the energy dispersion of the MQW sample *B* with 42 Å wide PbSe ($E_g = 146$ mev) layers and 253 Å wide $Pb_{1-x}Mn_xSe$ layers ($E_g = 206$ meV). The band parameters for the interband momentum matrix elements are those listed by Hofmann *et al.*[8] For the far band masses the values for PbSe were taken for both the

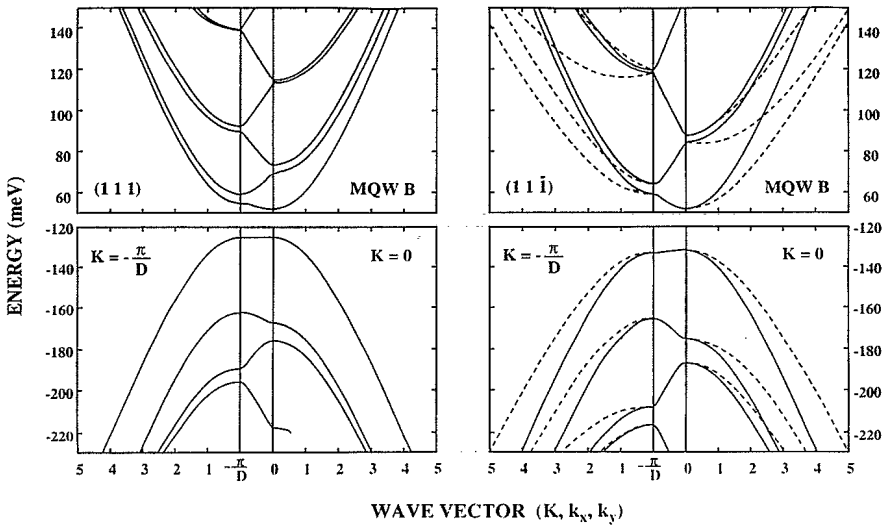

FIG. 3. Energy-momentum relationship calculated by the EFA model for $PbSe/Pb_{1-x}Mn_xSe$ for a normalized CB offset $\Delta E_c/\Delta E_g = -0.4$ for MQW *B*: longitudinal (111) valley (left-hand side) and oblique (11$\bar{1}$) valley (right-hand side) calculated from EFA. The dispersion along the superlattice growth direction (between $K = 0$ and $K = \pi/D$) is shown, as well as the dispersion as a function of $k_x \| [1\bar{1}0]$ and $k_y \| [11\bar{2}]$ (full lines and dashed lines, respectively). The origin of the energy scale is taken to be in the center of the material with the smaller energy gap, i.e., in the middle of the PbSe gap.

binary and the ternary compounds.[7] For the calculation a normalized conduction-band offset $\Delta E_c/\Delta E_g = -0.4$ was assumed, where ΔE_c denotes the difference of the conduction-band levels of $Pb_{1-x}Mn_xSe$ and PbSe and ΔE_g the difference of the respective energy gaps. Thus for the value of $\Delta E_c/\Delta E_g = -0.4$ the conduction-band level of the ternary compound $Pb_{1-x}Mn_xSe$ lies *below* that of the binary PbSe. The energy dispersion is shown for both the longitudinal valley [111] and the three oblique valleys $\langle 11\bar{1}\rangle$. The in-plane dispersion is shown as a function of k_x and k_y with $k_x \| [1\bar{1}0]$ (solid line) and $k_y \| [11\bar{2}]$ (dashed line) for $K=0$ and $K=\pi/D$, i.e., for the center and the edge of the mini BZ. Actually, due to the small effective masses, there is an appreciable dispersion in the energy momentum relationship along the [111] (z-)growth direction which is more pronounced for the oblique valleys due to the lighter masses involved in comparison to the longitudinal valleys. Thus the notation "MQW" does not mean that the carriers are confined for all levels in wells. In Fig. 3, the zero of the vertical energy scale is taken in the middle of the energy gap of PbSe.

In order to get some understanding of interband optical transitions in such a spatially *indirect* superlattice, it is quite useful to calculate carrier wave functions associated with several conduction and valence energy eigenstates both at $K=0$ and $K=\pi/D$. In Fig. 4, such calculations for the square of the carrier wave function $|\Psi|^2$ are shown for MQW sample B for the following sequence of levels: lowest part: valence band (VB), $i=1$ level, conduction band (CB) $i=1,2$, and 3 levels. According to this figure, there is a finite overlap of the wave functions of the $i=1$ subband in the valence band with the $i=1$ and 3 subbands of the conduction band, i.e., allowed transitions are expected whereas the transitions between the $i=1$ VB level and the $i=2$ CB level are practically forbidden at $K=0$, i.e., at the center of the mini BZ. This follows from Fig. 4(b) where the overlap of valence- [Fig. 4(d)] and conduction-band wave function nearly vanishes. It should be noticed that each level is twofold degenerate.

Based on the EFA model, the transition energies of allowed transitions were calculated as a function of the conduction-band offset in the range from $\Delta E_c/\Delta E_g = -1$ to 0. These data are shown for sample MQW B in Fig. 5. Since it is quite evident that electrons and holes are confined in the $Pb_{1-x}Mn_xSe$ and PbSe layers, respectively, from the previous CARS data,[9] this range of offsets is sufficient for further analysis of the experimental absorption and photoconductivity data. The strongest interband transitions are shown for $K=0$ and for $K=\pi/D$ involving energy states in the longitudinal and oblique valleys. Due to the complicated superlattice band structure and the finite miniband width, transitions at the edge of the mini BZ turn out to be equally important as those at the center. In a type-I band alignment the strongest in-

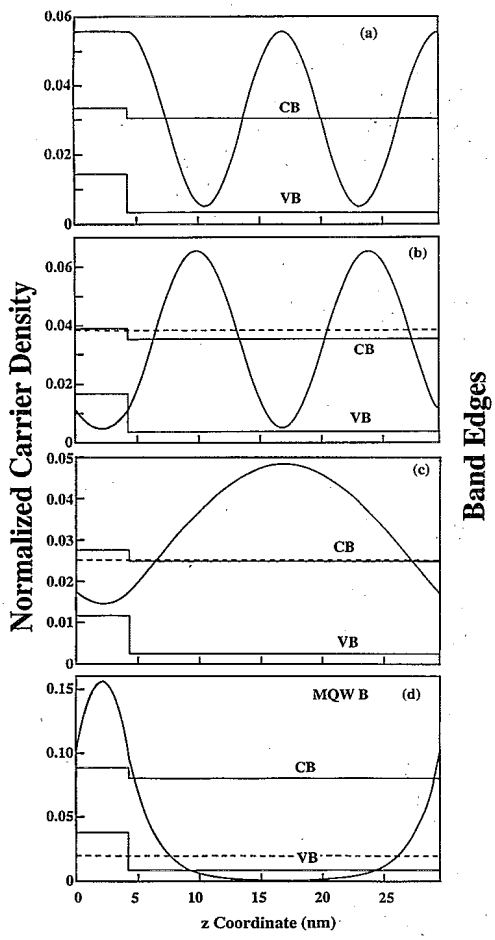

FIG. 4. Normalized carrier density in sample MQW B calculated by the EFA method for various subbands of longitudinal valley at $K=0$: (a) VB, $i=1$, (b) CB, $i=1$, (c) CB, $i=2$, and (d) CB, $i=3$. The dashed lines show the lowest energy states of the minibands, the full lines the band edge profiles.

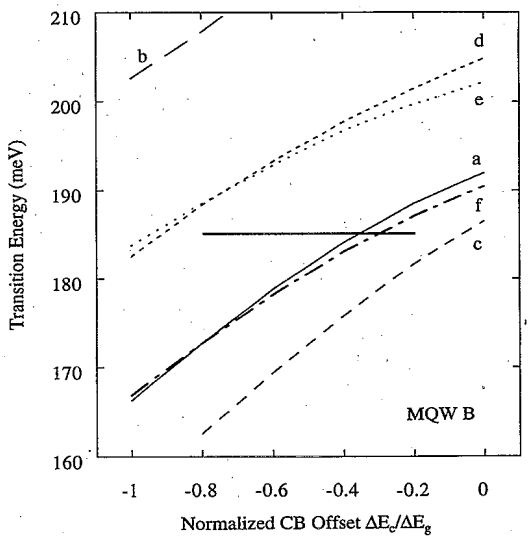

FIG. 5. Strong interband transitions as a function of the normalized CB offset calculated by the EFA method at the SL's miniband centers ($K=0$) and edges ($K=\pi/D$). The transitions involving electrons in the longitudinal valleys are indicated by letters "*a*" ($V1\rightarrow C2, K=\pi/D$), "*b*" ($V1\rightarrow C4, K=\pi/D$), "*c*" ($V1\rightarrow C1, K=0$), and "*d*" ($V1\rightarrow C3, K=0$), and in the oblique valleys by "*e*" ($V1\rightarrow C2, K=\pi/D$) and "*f*" ($V1\rightarrow C1, K=0$). The straight solid line in the middle of the graph indicates the strongest transition observed in the experiments for MQW sample B.

terband transitions are those with $\Delta i = 0$ (in a rectangular modulated quantum-well structure), where i denotes the subband index. In the staggered band structure, transitions for which $\Delta i \neq 0$ turn out to be equally important as demonstrated by Fig. 5. Furthermore, it is important to remember that the oblique valleys have a threefold valley degeneracy which enters the calculation for the absorption coefficient.

IV. OPTICAL PROPERTIES: TRANSMISSION AND PHOTOCONDUCTIVITY

It is well known that, in staggered type-II superlattice, the absorption coefficient increases with photon energy rather smoothly,[16–18] whereas, in type-I superlattices, it reflects the steplike shape of the joint density of states. Therefore, transitions between distinct energy levels of the valence and conduction bands are much more difficult to observe and to assign in samples with a staggered band lineup. Consequently, we did not use only transmission, but also photoconductivity experiments to get information on the onset of absorption as well as any changes due to higher transitions. In addition, to increase the sensitivity of transmission experiments with respect to interband transitions, the transmission of the MQW samples was recorded at $T = 5$ K and afterwards at $T = 21$ K. By normalizing their difference to the transmission at 5 K ($\Delta T/T$), the onset of interband absorption and changes due to further strong interband transitions could be deduced from the experiments.

In Fig. 6, upper half, typical results of both the photoconductivity spectrum and the $\Delta T/T$ spectrum are shown for MQW B. The corresponding transmission spectrum is shown in Fig. 7. The interference fringes in the transmission result from the change of refractive index at the semiconductor layer-substrate and the semiconductor layer-vacuum interface. The transmission maximum at about 1300 cm^{-1}, i.e., above the PbSe energy gap is much higher than that at about 1520 cm^{-1}, which coincides with the $(1-1)^o$ transition and is consequently smaller in amplitude due to the finite absorption. The energy gap of the buffer layer $Pb_{1-x}Mn_xSe$, which has the same x content as the ternary layers in the MQW structure, is shown as well. The buffer causes the strong decrease in transmission beyond 1700 cm^{-1}.

The photoconductivity and transmission data are analyzed using a model that was described recently by us.[15,19,20] The EFA model is not only used to calculate the energy eigenstates and wave functions, but also to calculate directly the frequency dependence of the absorption coefficient $\alpha(\omega)$, by an integration in $\mathbf{k}$ (k_x,k_y,K) space over the possible interband transitions. This $\alpha(\omega)$ is thus related to the imaginary part $\delta\varepsilon_2^{\text{VB-CB}}$ of the dielectric function by[15,17]

$$\delta\varepsilon_2^{\text{VB-CB}} = (cn/\omega)\alpha = \frac{4\pi^2 e^2}{\omega^2}\frac{1}{(2\pi)^3}\int d^3\mathbf{k}\,\delta(E_f - E_i - h\omega) \times |\langle f|\dot{r}_E|i\rangle|^2 (f_i - f_f)\,, \quad (1)$$

where E_i and E_f denote the energies of the initial state (i)

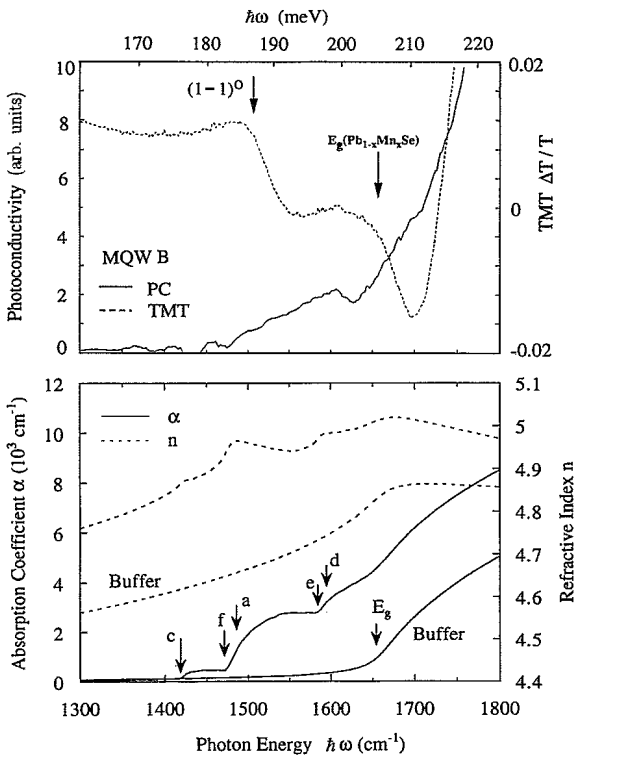

FIG. 6. Upper panel: Photoconductivity (solid line, $T = 5$ K) and temperature modulated transmission spectra of MQW B {$[T(21\text{ K})-T(5\text{ K})]/T(5\text{ K})$, dashed line}. The frequency dependence is representative for a staggered type of band lineup. Note the absence of steplike features in comparison to the $PbTe/Pb_{1-x}Eu_xTe$ MQW's (see Fig. 8) due to type-II behavior. Lower panel: Calculated absorption coefficients (solid lines) and refractive indices (dashed lines) of the buffer layer and for the MQW (sample B). A normalized CB offset of -0.4 was used in the calculation. Arrows indicate various transitions at $K = 0$ and $K = \pi/D$ (see Fig. 5 for the definition of the letters "a," "f," etc.)

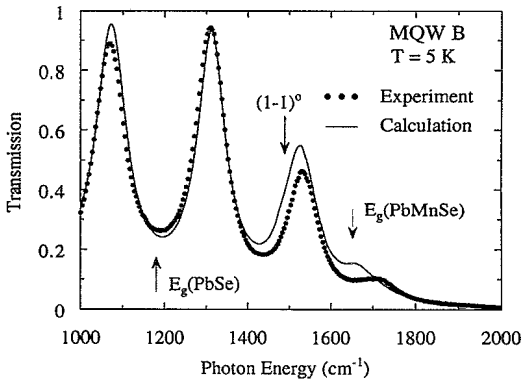

FIG. 7. Experimental and EFA calculated transmission spectra of sample MQW B. Dots, experiment; solid line, calculation using a normalized CB offset of -0.4 without any adjustable parameters. Fringes are due to multireflection and interference effect in the whole MQW structure and the buffer on the BaF_2 substrate. Arrows indicate the energy gaps of PbSe and $Pb_{1-x}Mn_xSe$ and the strongest transition $(1-1)^o$ in the quantum-well structure identified by the temperature modulated transmission and photoconductivity measurements (see Fig. 6). "o" stands for oblique valleys.

and final state (f) and f_i, f_f denote the Fermi-Dirac distribution functions for the occupancy of the initial and final states. We emphasize that the refractive index n cancels out in the expression for $\delta\varepsilon_2^{\text{VB-CB}}$ in Eq. (1). In the derivation of Eq. (1) it was assumed that the superlattice is optically homogeneous. This is a reasonable approximation in view of the fact that the wavelength of the radiation is much larger than the PbSe and/or $Pb_{1-x}Mn_xSe$ layer widths.

In the EFA the velocity operator is given by

$$\dot{\mathbf{r}}=\frac{1}{ih}[\mathbf{r},H]=\frac{1}{h}\frac{\partial H}{\partial \mathbf{k}} . \tag{2}$$

Equation (1) was evaluated numerically for the three MQW samples by calculating their energy dispersion and wave functions for a sufficient number of points in (k_x,k_y,K) space.

From this imaginary part, the real part $\delta\varepsilon_1^{\text{VB-CB}}$ is determined by a Kramers-Kronig transformation:

$$\delta\varepsilon_1^{\text{VB-CB}}=\frac{2}{\pi}P\int_0^\infty d\omega'\omega'\delta\varepsilon_2^{\text{VB-CB}}(\omega')/(\omega'^2-\omega^2) . \tag{3}$$

The upper limit, i.e., infinity, is replaced with ω_c, the cutoff frequency in the integration of the Kramers-Kronig transformation. The cutoff frequency ω_c is chosen such that the line shape of $\delta\varepsilon_1^{\text{VB-CB}}$ in the photon energy range from 1000 to 2000 cm^{-1}, which is due to the transitions at the fundamental L_6^+ to L_6^- gap, no longer changes with increasing cutoff frequency. It turned out that this cutoff frequency is approximately the frequency corresponding to E_g+3000 cm^{-1}. Any cutoff frequency beyond this value does not affect the shape of $\delta\varepsilon_1^{\text{VB-CB}}$ in the frequency range from 1000 to 2000 cm^{-1}. However, the magnitude of $\delta\varepsilon_1^{\text{VB-CB}}$ in this frequency range still increases with increasing cutoff frequency. The total dielectric function ε^{tot} from which the total absorption coefficient and refractive index are obtained, requires the knowledge of the background dielectric function ε^{BG}, which is obtained from measurements on PbSe and $Pb_{1-x}Mn_xSe$ epitaxial layers.

The expressions

$$\begin{aligned}\varepsilon^{\text{tot}}&=\varepsilon_1^{\text{tot}}+i\varepsilon_2^{\text{tot}}\\&=(\varepsilon_1^{\text{BG}}+\delta\varepsilon_1^{\text{VB-CB}})+i(\varepsilon_2^{\text{BG}}+\delta\varepsilon_2^{\text{VB-CB}})\end{aligned} \tag{4}$$

are used in the following. Similar to our previous work on PbTe and $Pb_{1-x}Eu_xTe$ epilayers,[19] in the range from 1000 to 2000 cm^{-1} we neglect $\varepsilon_2^{\text{BG}}$ and treat $\varepsilon_1^{\text{BG}}$ as a quadratic function of photon energy to account for the contribution of any absorptions at critical points other than that at the fundamental absorption. $\varepsilon_1^{\text{BG}}(\omega)$ was determined from fits to the experimental transmission spectra of PbSe and $Pb_{1-x}Mn_xSe$ ($x=1.3\%$) epilayers. We found that in the range from 1000 to 2000 cm^{-1}, the expression

$$\varepsilon_1^{\text{BG}}=24+1.5\times10^{-7}\ (h\omega)^2/(\text{cm}^{-1})^2$$

holds for PbSe and

$$\varepsilon_1^{\text{BG}}=19.5+7.7\times10^{-7}\ (h\omega)^2/(\text{cm}^{-1})^2$$

for $Pb_{1-x}Mn_xSe$ with $x=1.3\%$. Extrapolated $\varepsilon_1^{\text{BG}}$ values were used for the $Pb_{1-x}Mn_xSe$ layers of the PbSe/$Pb_{1-x}Mn_xSe$ quantum-well samples with other x values. Since $\varepsilon_1^{\text{BG}}$ excludes the contribution from the fundamental absorption at the minimum gap, it is not identical to the high-frequency dielectric constant ε_∞. Optical properties of PbSe were also studied recently by Hermann and co-workers.[21,22]

As shown in Fig. 4, the contributions from the interband electronic transitions to the optical constants extend throughout the entire PbSe/$Pb_{1-x}Mn_xSe$ structure. Actually, in the EFA calculation, the contribution from the interband transitions $\delta\varepsilon_2^{\text{VB-CB}}$ is the same and thus also $\delta\varepsilon_1^{\text{VB-CB}}$ is the same for the PbSe and $Pb_{1-x}Mn_xSe$ layers, whereas the background contributions $\varepsilon_1^{\text{BG}}$ are different, as mentioned above.

For the calculation of the transmission of the superlattice as a function of frequency, the transfer-matrix method was employed.[23] For the calculation of the optical properties of the PbSe/$Pb_{1-x}Mn_xSe$ structures, the effective medium approach[24] was used. This is fully justified for normal incidence of the electromagnetic radiation and keeping in mind that the *wavelength* in the frequency range from 1300 to 1800 cm^{-1} is *larger* by a factor of about 30 than the superlattice period for a refractive index of approximately 5. Treating the SL as an effective medium, the total dielectric function is averaged over one SL period according to:

$$\varepsilon_1^{\text{tot(SL's)}}=\frac{d_{\text{PbSe}}\varepsilon_1^{\text{tot}(PbSe)}+d_{Pb_{1-x}Mn_xSe}\varepsilon_1^{\text{tot}(Pb_{1-x}Mn_xSe)}}{d_{\text{PbSe}}+d_{Pb_{1-x}Mn_xSe}} . \tag{5}$$

In this spirit, for the calculation of the transmission, the transfer-matrix method was used for the sequence of layers: BaF_2 substate, $Pb_{1-x}Mn_xSe$ buffer, and PbSe/$Pb_{1-x}Mn_xSe$ SL structure. Thus the SL structure was treated as an optically homogeneous medium with the total thickness ND, where N denotes the number of SL periods.

In Fig. 6, in the lower half, $\alpha(\omega)$ and $n(\omega)$ for the SL layers of the MQW sample B are shown together with the corresponding data for the $Pb_{1-x}Mn_xSe$ buffer layer. The absorption constant reflects the various interband transitions shown in Fig. 5 and marked by the letters a–f. The strongest one, f, is due to the $(1-1)^o$ transition at $K=0$. It is also reflected in a cusp in the $n(\omega)$ relationship. We notice, that the photoconductivity signal, as shown in the upper part of Fig. 6 reflects very well the dependence of α on ω. The oscillator strength of the transition $(1-2)^l$ at $K=\pi/D$ (denoted by letter a in Figs.

5 and 6) is similar to that of the transition f. Their relative values are 7×10^{15} (arbitrary units) and 6×10^{15} (arbitrary units), respectively. However, due to the threefold degeneracy of the oblique valleys, f is much stronger than a. The oscillator strengths of transition c, $(1-1)^l$ at $K=0$, and transition d, $(1-3)^l$ at $K=0$, are smaller by a factor of $6(=3\times2)$ than that of f, so they are very weak. The oscillator strength of transition e, $(1-2)^o$ at $K=\pi/D$, is smaller than that of f, but the transition energy is close to the energy gap of the $Pb_{1-x}Mn_xSe$ buffer. Therefore, this transition is hard to distinguish from the tail of the absorption of the thick buffer layer in the experiments. By using the calculated optical constants $\alpha(\omega)$ and $n(\omega)$ for the SL and those measured for the $Pb_{1-x}Mn_xSe$ buffer layer and the BaF_2 substrate, the calculated transmission data of Fig. 7 were obtained without any fit parameter. The main cause of the interference fringes in the transmission spectrum are the changes of the refractive index at the BaF_2/semiconductor layer interface and the layer-vacuum interface. The envelope of the fringes reflects the frequency dependence of $\alpha(\omega)$ in the SL structure and in the $Pb_{1-x}Mn_xSe$ buffer.

The photoconductivity spectrum shown in Fig. 6 is quite representative of the other samples as well, apart from changes in the onset frequency due to the different layer thicknesses of samples A and C. The photoconductivity spectra for a type-I superlattice of another combination of IV-VI compounds with a similar bulk band structure ($PbTe/Pb_{1-x}Eu_xTe$ MQW sample, $x=2.4\%$, 118-Å PbTe well width, 486-Å barrier width, 30 periods) is *qualitatively different*. It reflects in its frequency dependence the steplike changes in the density of states [as shown here for $(1-1)^l$, $(2-2)^l$, $(3-3)^l$, and $(1-1)^o$ transitions]. The photoconductivity response follows very well the frequency dependence of the absorption constant which was calculated for this $PbTe/Pb_{1-x}Eu_xTe$ MQW sample from a similar EFA approach.

The comparison between Figs. 6 and 8 demonstrates

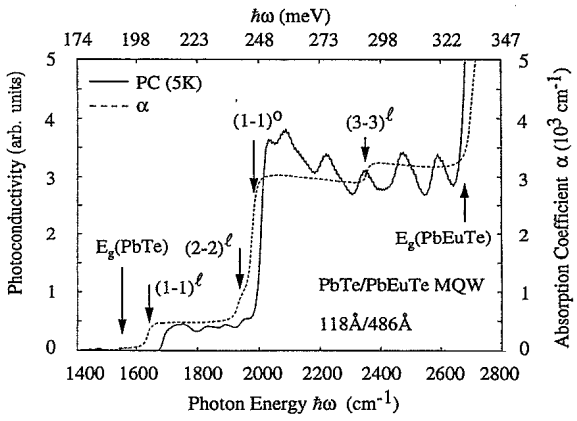

FIG. 8. Photoconductivity spectrum (solid line) and EFA calculated absorption coefficient (dashed line) for a 118 Å/486 Å $PbTe/Pb_{1-x}Eu_xTe$ MQW sample (type I). The steplike line shape clearly seen here is not observed for the $PbSe/Pb_{1-x}Mn_xSe$ samples (type II), both experimentally and theoretically. The fringes in the photoconductivity spectrum are due to Fabry-Pérot oscillations.

quite clearly the consequences of the type-II band alignment for the photoconductivity spectrum which is in strong contrast to that for a type-I band alignment.

V. BAND OFFSETS

For the three samples listed in Table I, photoconductivity spectra, transmission spectra, and $\Delta T/T$ spectra were taken and analyzed with the calculated absorption coefficients as outlined above. A comparison of the interband transition energies deduced from the experiments with the strongest calculated transitions is shown in Fig. 9, in the latter case as a function of normalized conduction-band offset. The overall agreement between experiment and calculation is best for an offset of $\Delta E_c/\Delta E_g$ of about -0.4 to -0.6 (±0.2). Thus the absorption and photoconductivity data are in agreement with the previous CARS experiments,[9] i.e., the holes are confined to PbSe layers whereas the electrons are confined to the $Pb_{1-x}Mn_xSe$ layers in the $PbSe/Pb_{1-x}Mn_xSe$ SL structures.

The MQW samples A, B, and C cover the range of Mn contents from 0.8% to 1.6%, i.e., the manganese content varies by a factor of 2. By close inspection of Fig. 9 one may suspect that the normalized conduction-band offset $\Delta E_c/\Delta E_g$ is not constant but varies somewhat with Mn content from -0.6 for sample C (0.8%) to -0.4 for samples A and B (1.5% and 1.6%). Such a dependence of the offset on Mn composition is not *a priori* improbable. On the contrary, e.g., the variation of the band offset with In content is well documented for the MQW system $GaAs/Ga_{1-x}In_xAs$ where in the range from $x=0.05$ to $x=0.15$ the conduction-band offset changes from 0.4 to 0.8.[25–27] For the case of $PbSe/Pb_{1-x}Mn_xSe$, as for $GaAs/Ga_{1-x}In_xAs$, investigations on a large number of samples with different Mn contents would be necessary in order to deduce quantitatively the dependence of the conduction-band offset on the Mn content. The different Mn content in the $Pb_{1-x}Mn_xSe$ layers of samples A, B, and C induces a different strain status, too. However, the optical properties of the $PbSe/Pb_{1-x}Mn_xSe$ MQW's were studied at $T=5$ K and thus the additional biaxial tensile strain due to the thermal mismatch between the BaF_2 substrate and the IV-VI compound layers dominates completely the one due to lattice constant mismatch,[10] and thus with respect to the strain status, the MQW samples A, B, and C are nearly identical. The strain-induced splittings of the L conduction- and valence-band states amount only to a small fraction of the band offsets and is well below the experimental uncertainty of the determination of $\Delta E_c/\Delta E_g$.

VI. CONCLUSION

Optical properties of $PbSe/Pb_{1-x}Mn_xSe$ MQW and SL structures were investigated by midinfrared transmission and by photoconductivity measurements. The staggered band lineup in this system leads to a rather moderate increase of the absorption constant with frequency, in the range of interband transitions between

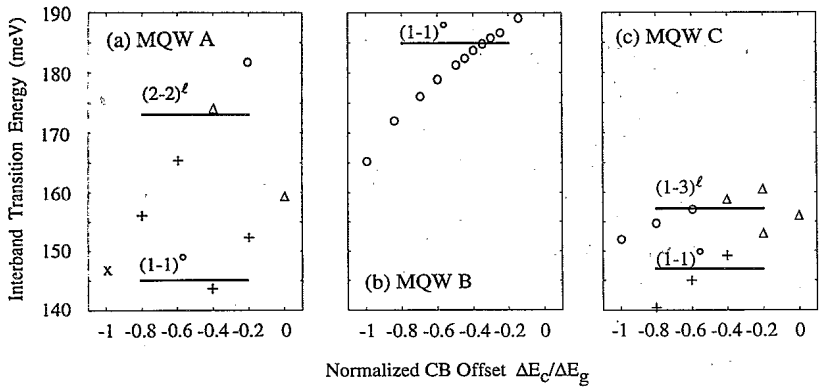

FIG. 9. Comparison of the experimentally determined interband transition energies (straight solid lines) with those (markers) of EFA calculation as a function of the normalized CB offset $\Delta E_c/\Delta E_g$ for sample *A* (a), *B* (b), and *C* (c). Symbols ○, △, +, and × denote different transition probabilities decreasing stepwise by a factor of 2.

confined levels, or minibands of the valence and conduction band. This behavior is in contrast to that found in PbTe/$Pb_{1-x}Eu_xTe$ MQW's which have a type-I band alignment and show a steplike increase of $\alpha(\omega)$. Envelope-function approximation calculations were used to calculate the energy eigenstates, the corresponding carrier wave functions and the oscillator strengths of the interband transitions. From an integration in **k** space also the absorption constant is determined which is used further to obtain the contribution of the VB-CB transitions, at the fundamental gap, to the real part of the dielectric constant, by performing the proper Kramers-Kronig transformation. In samples with finite miniband width, it turns out that $\alpha(\omega)$ is, as expected, determined by transitions at both $K=0$ and $K=\pi/D$, i.e., at the center and at the edges of the mini Brillouin zone. The staggered band structure leads also to an appreciable oscillator strength for transitions between valence- and conduction-band states with different subband index, i.e., $\Delta i \neq 0$. From the calculated $\alpha(\omega)$ and $n(\omega)$, the frequency dependence of the transmission was calculated and compared with experimental data. For this calculation, an effective medium approach was used, i.e., the dielectric function of the superlattice is obtained from a weighted mean average of the PbSe and $Pb_{1-x}Mn_xSe$ dielectric functions. The contribution of the interband transitions of the valence electrons $\delta\varepsilon_2^{\text{VB-CB}}$ was calculated by EFA. The effective medium approach is well justified, since in the frequency range of interest close to the fundamental interband transition energies, the wavelength of the electromagnetic radiation is about a factor of 30 larger than the superlattice period *D*. Using the known band parameters of PbSe and $Pb_{1-x}Mn_xSe$ and the structural parameters of the SL samples, the calculated transmission spectra agree very well with the experimental ones, without using *any* adjustable parameters.

ACKNOWLEDGMENTS

Work supported by Fonds zur Förderung der Wissenschaftlichen Forschung, Vienna, Austria. We thank G. Springholz for the MBE growth of the PbTe/$Pb_{1-x}Eu_xTe$ MQW sample, E. Koppensteiner and H. Krenn for helpful discussions, and M. Seto for a critical reading of the manuscript.

[1]H. Preier, Semicond. Sci. Technol. **5**, S12 (1990).
[2]D. L. Partin, IEEE J. Quantum Electron. **QE-24**, 1716 (1988).
[3]Z. Feit, D. Kostyk, R. J. Woods, and P. Mak, Appl. Phys. Lett. **58**, 343 (1991).
[4]M. Tacke, B. Spanger, A. Lambrecht, P. R. Norton, and H. Böttner, Appl. Phys. Lett. **53**, 2260 (1988).
[5]K. H. Schlereth, B. Spanger, H. Böttner, A. Lamrecht, and M. Tacke, Infrared Phys. **30**, 449 (1990).
[6]I. I. Zasavitskii, L. Kowalczyk, B. N. Matsonashvili, and A. V. Sazonov, Fiz. Tekh. Poluprovodn. **22**, 2118 (1988) [Sov. Phys. Semicond. **22**, 1338 (1988)].
[7]H. Pascher, G. Bauer, and R. Grisar, Phys. Rev. B **38**, 3383 (1988).
[8]W. Hofmann, U. Fichtel, H. Pascher, N. Frank, and G. Bauer, Phys. Rev. B **45**, 8742 (1992).
[9]F. Geist, H. Pascher, N. Frank, G. Bauer, and M. Kriechbaum, Semicond. Sci. Technol. **8**, S147 (1993).
[10]M. Kriechbaum, P. Kocevar, H. Pascher, and G. Bauer, IEEE J. Quantum Electron. **QE-24**, 1727 (1988).
[11]N. Frank, A. Voiticek, H. Clemens, A. Holzinger, and G. Bauer, J. Cryst. Growth **126**, 93 (1993).
[12]N. Koguchi, S. Takahashi, and T. Kiyosawa, Jpn. J. Appl. Phys. **27**, 2376 (1988).
[13]P. F. Fewster, Semicond. Sci. Technol. **8**, 1915 (1993).
[14]G. Springholz, G. Ihninger, G. Bauer, M. M. Olver, J. Z. Pastalan, S. Romaine, and B. B. Goldberg, Appl. Phys. Lett. **63**, 2908 (1993).
[15]S. Yuan, G. Springholz, G. Bauer, and M. Kriechbaum, Phys. Rev. B **49**, 5476 (1994).
[16]L. L. Chang, G. A. Sai-Halasz, L. Esaki, and R. L. Aggarwal, J. Vac. Sci. Technol. **19**, 589 (1981).
[17]N. F. Johnson, H. Ehrenreich, P. M. Hui, and P. M. Young, Phys. Rev. B **41**, 3655 (1990); P. M. Young, P. M. Hui, and H. Ehrenreich, *ibid.* **44**, 12 969 (1991).
[18]I. H. Campbell, I. Sela, B. K. Laurich, D. L. Smith, C. R. Bolognesi, L. A. Samoska, A. C. Gossard, and H. Kroemer,

Appl. Phys. Lett. **59**, 846 (1991).
[19]S. Yuan, H. Krenn, G. Springholz, and G. Bauer, Phys. Rev. B **47**, 7213 (1993).
[20]S. Yuan, H. Krenn, G. Springholz, G. Bauer, and M. Kriechbaum, Appl. Phys. Lett. **62**, 885 (1993).
[21]K. H. Herrmann, U. Müller, and V. Melzer, Semicond. Sci. Technol. **8**, S331 (1993).
[22]K. H. Herrmann and A. F. Rudolph, Infrared Phys. **33**, 66 (1992).
[23]A. F. Terzis, X. C. Liu, A. Petrou, B. D. McCombe, M. Dutta, H. Shen, Doran D. Smith, M. W. Cole, M. Taysing-Lara, and P. G. Newman, J. Appl. Phys. **67**, 2501 (1990).
[24]P. Appel and O. Hunderi, in *Optical Properties of Superlattices, Handbook of Optical Constants II,* edited by E. D. Palik (Academic, Boston, 1991), p. 97.
[25]M. J. Joyce, M. J. Johnson, M. Gal, and B. F. Usher, Phys. Rev. B **38**, 10 978 (1988).
[26]S. H. Pan, H. Shen, Z. Hang, F. H. Pollack, W. Zhuang, Q. Xu, A. P. Roth, R. A. Massut, C. Lacelle, and D. Morris, Phys. Rev. B **38**, 3375 (1988).
[27]J. Y. Marzin, J. M. Gerard, P. Voisin, and J. A. Brum, in *Semiconductors and Semimetals,* edited by T. P. Pearsall (Academic, Boston, 1990), Vol. 32, p. 56, and references cited therein.